nature energy

Article

https://doi.org/10.1038/s41560-022-01167-7

High-performing organic electronics using terpene green solvents from renewable feedstocks

Received: 9 June 2022

Accepted: 24 October 2022

Published online: 15 December 2022

Check for updates

Daniel Corzo, Diego Rosas-Villalva, Amruth C, Guillermo Tostado-Blázquez, Emily Bezerra Alexandre, Luis Huerta Hernandez, Jianhua Han, Han Xu, Maxime Babics, Stefaan De Wolf & Derya Baran

Accelerating the shift towards renewable materials and sustainable processes for printed organic electronic devices is crucial for a green circular economy. Currently, the fabrication of organic devices with competitive performances is linked to toxic petrochemical-based solvents with considerable carbon emissions. Here we show that terpene solvents obtained from renewable feedstocks can replace non-renewable environmentally hazardous solvent counterparts in the production of highly efficient organic photovoltaics (OPVs) light-emitting diodes (OLEDs) and field-effect transistors (OFETs) with on-par performances. Using a Hansen solubility ink formulation framework, we identify various terpene solvent systems and investigate effective film formation and drying mechanisms required for optimal charge transport. This approach is universal for state-of-the-art materials in OPVs, OLEDs and OFETs. We created an interactive library for green solvent selections and made it publicly available through the OMEGALab website. As potential carbon-negative solvents, terpenes open a unique and universal approach towards efficient, large-area and stable organic electronic devices.

The transition from fossil-based resources to renewables to mitigate climate change is a key challenge of the twenty-first century. Organic electronics (OEs) using carbon-based conjugated polymers and small molecules produce fewer carbon emissions in comparison with their inorganic counterparts[1]. The consensus to propel organic semiconductors (OSCs) into a circular economy prioritizes the use of renewable and abundant materials, weeding out toxic chemicals, following sustainable manufacturing practices and designing routes for recycling and end-of-life biodegradation. Despite this, the synthesis and processing of state-of-the-art materials heavily relies on petrochemical-based ingredients and halogenated solvents for cross-coupling reactions and purification and to form optimal morphologies leading to record performances[2,3].

There have been some efforts at utilizing biomass-derived monomers and modifying the synthetic routes of OSCs[4,5]. However, the carbon emissions of halogenated solvents, in addition to their toxicological effects such as reproductive hazards and cancer, pose a serious risk to human safety and the environment, rendering them unsustainable for high-throughput fabrication of solution-based electronic devices[6,7]. Recent strategies to transition towards environmentally friendly solvents require either the modification of OSC sidechains to improve solubility[8–10], the utilization of hydrocarbon solvents along with additives like diphenyl ether to boost performance[11–13] or the calculation of Hansen solubility parameters (HSP) to methodical filter potential solvent candidates for processing[14–17]. Yet, these strategies were limited to five standard hydrocarbon-based solvents: xylene, toluene, trimethylbenzene, o-methylanisole and tetrahydrofuran. Nonetheless, matching the solubility, morphology and charge transport required for on-par performance (to commonly used toxic solvents) with out-of-norm non-aromatic solvents is a persistent conundrum.

Physical Sciences and Engineering Division, KAUST Solar Center (KSC), King Abdullah University of Science and Technology (KAUST), Thuwal, Saudi Arabia. e-mail: derya.baran@kaust.edu.sa

Additionally, trade-offs between solubility, evaporation, large-scale processability, toxicity and environmental impact through potential carbon footprint are seldom addressed.

HSP is a quantitative model based on the representation of solubility as 3D spheres in a complex space defined by the dispersive (δD), polar (δP) and hydrogen-bonding (δH) intermolecular forces. It is used extensively for alternative solvent selection in the coating, hygiene and food industries[18,19]. Correspondingly, it can provide a framework to address the solubility performance challenges of OSCs with alternative renewable and non-toxic biosolvents based on three criteria: first, the organic components solubility spheres (SS) should be defined, and non-toxic solvent candidates should be filtered based on their distance to the SS centre; second, the film formation kinetics should be studied as a function of solubility and evaporation behaviour; third, solvents should be cheap, have high boiling points (BPs) compatible with roll-to-roll processing (130–210 °C) and be produced from renewable carbon-recycling feedstocks like plants and algae to transition towards a sustainable circular economy.

Herein, using HSP, we identify a family of terpene solvents (eucalyptol (Eu), d-limonene (Lim), β-Pinene (Pin) and L-Menthone (Men)) as high-performing green inks for a variety of OE devices (organic photovoltaics (OPVs), light-emitting diodes (OLEDs) and field-effect transistors (OFETs)). These solvents present toxicities resembling human-consumable substances (median lethal dose (LD_{50}) > 2,500 mg kg^{-1}) and have the potential to become carbon negative as they are extracted from renewable biosources that valorize carbon (that is, plant waste and biorefineries) (Fig. 1a). We calculate the SS of state-of-the-art OE material systems to formulate binary green solvent compositions and analyse the effects of evaporation, HSP affinity and solubility dynamics on film morphology, charge transport and recombination via in situ spectroscopy and electronic characterization. We demonstrate the universality of terpene biosolvents for OE by fabricating OPV devices based on PM6:BTP-eC9, P3HT:O-IDTBR, PTB7-Th:IEICO-4F, PM6:IT-4F, PM6:PYT and PM6:PY-IT:BTP-eC9, OLED devices based on Super Yellow and green Livilux and *n*-type OFETs based on O-IDTBR and 2PyDPP-2CNTVT, with on-par performance merits as those fabricated from toxic solvents such as chloroform (CF). Furthermore, we validate the scalability of terpene solvent utilization by fabricating efficient large-area OPV devices (2.4 cm^2 single device (12.4%) and a 12 cm^2 five-cell module (9.1%), reporting real-life performance outdoors in the Kingdom of Saudi Arabia for 90 days.

Terpene biosolvents for circular carbon organic electronics

The circular carbon economy (CCE), endorsed by G20 countries, aims to manage emissions by pushing for technologies to remove, store and turn CO_2 into value-added products. Terpene biosolvents already constitute a green alternative as renewable feedstocks for chemical manufacturing and specialty biofuels[20–22]. Figure 1a outlines how the production of OEs such as OPVs, OLEDs and OFETs can provide an additional CO_2 valuation route in line with CCE initiatives by reducing excess emissions of halogenated solvents removing atmospheric CO_2 through biomass, reusing carbon through terpene production, recycling it for the synthesis of OSCs and providing cleaner means for energy harvesting. The consensus on transitioning OE towards non-halogen, non-aromatic solvents and alcohols is updated in Fig. 1b and Supplementary Fig. 1 with the inclusion of terpene solvents with HSP values resembling halogenated solvents (which are conventionally used to obtain high device performances) and toxicity limits resembling table salt (LD_{50} > 2,500 mg kg). The terpene selection methodology based on Hansen SS and respective relative energy differences (REDs) to desired OSC materials is described in Supplementary Information.

Terpenes occur naturally in plants, algae and other organisms to perform a wide range of biological functions. Due to their strong pleasant odours and medicinal properties, they are used in perfumes, cosmetics, food flavourings, cleaning products and drugs[23]. As they can be produced through distillation and solvent extraction from leaves, flowers and fruits, they present a lower carbon footprint than conventionally utilized solvents (0.4 for Lim versus 3.4 kg CO_2 equivalent (CO_2 eq.) kg^{-1} for CF) (Fig. 1c)[24,25]. Moreover, terpenes have the potential to become carbon negative through enzymatic biosynthetic processes from algae, fungi and bacteria[26–28]. A summary of literature reports on greener solvent transition for OPVs, OLEDs and OFETs is given in Fig. 1d–f and expanded in Supplementary Fig. 2 and Supplementary Tables 1–3. It gives a comprehensible comparison of the performance for each device versus the toxicity and classification of the solvents utilized for their fabrication. There is a trend to transition towards lower-toxicity solvents, although the utilization of truly renewable alternatives to produce efficient OEs has been scarcely demonstrated.

HSP-driven ink formulation and film formation mechanisms

Hansen solubility provides a powerful solvent selection platform for any OSC, and thus, we first prove its applicability to formulate renewable inks for state-of-the-art OPV materials such as donor PM6 (PBDB-T-2F) and non-fullerene acceptor (NFA) BTP-eC9 (a member of the Y series; Supplementary Scheme 1). This particular blend has yielded record efficiencies (certified 17.3%) (ref. [29]); however, it suffers from poor solubility in non-halogenated solvents due to its conjugated nature[30]. Figure 2a shows the SS and HSP values of both components, which were calculated experimentally through the binary gradient methodology (Supplementary Scheme 2 and Supplementary Fig. 3) and methodically through group contribution means (Supplementary Scheme 3 and Supplementary Tables 4 and 5)[14,31]. We analysed more than 10,000 industrial solvents through the HSPiP software (Supplementary Fig. 4) and ranked them by LD_{50} and boiling point (BP) (Supplementary Fig. 5 and Supplementary Table 6). Additionally, we extended the GlaxoSmithKline (GSK) solvent selection guide to rank common terpene solvents in categories including waste, health, safety and environmental impact based on a globally harmonized system of classification and labelling of chemicals (Supplementary Table 7)[32,33].

We utilized the HSP linear additive behaviour to prepare terpene-based binary solvent formulations with the shortest distance to the donor SS: eucalyptol:tetralin (Eu:Tet), limonene:indan (Lim:Ind), pinene: ethyl phenyl sulfide (Pin:EPS) and menthone:tetralin (Men:Tet), with co-solvents denoted as potential solvent composition lines in Hansen space (Supplementary Fig. 6). As the BTP-eC9 SS encloses that of PM6, the formulation process is designed with the donor solubility as the limiting factor. The terpene solvents (Eu, Lim, Men and Pin) sit at the edges of the PM6 SS, thus only a small portion (<0.1 mg ml^{-1}) can be dissolved (Supplementary Fig. 7). The addition of a higher co-solvent percentage (Tet, Ind, EPS) moves the formulation HSP along the solvent composition lines and closer to the PM6 SS centre, increasing its solubility limit (Fig. 2b). The optimal volumetric formulations, HSP and RED values to PM6 and BTP-eC9 are listed in Supplementary Table 8.

The right schematic in Fig. 2c summarizes how Hansen solubility is used as a tool to engineer ink formulations and control the film drying kinetics to ensure a favourable morphology. The left panel shows the four stages of the bulk-heterojunction formation process as the formulation moves across the solvent composition line in Hansen space with the evaporation of the low-BP terpene solvent and the high-BP co-solvent. We defined solubility affinity (A_{sol}) in Fig. 2d as the closeness of the solvent to either donor or acceptor molecules in Hansen space (equation (1)).

$$A_{sol} = \frac{R_a \text{ solvent to donor} - R_a \text{ solvent to acceptor}}{R_a \text{ donor to acceptor}} \quad (1)$$

If $A_{sol} > 0$, then the solvent is closer to the acceptor than the donor; $A_{sol} < 0$ means the solvent is closer to the donor; and $A_{sol} = 0$ means the

https://doi.org/10.1038/s41560-022-01167-7

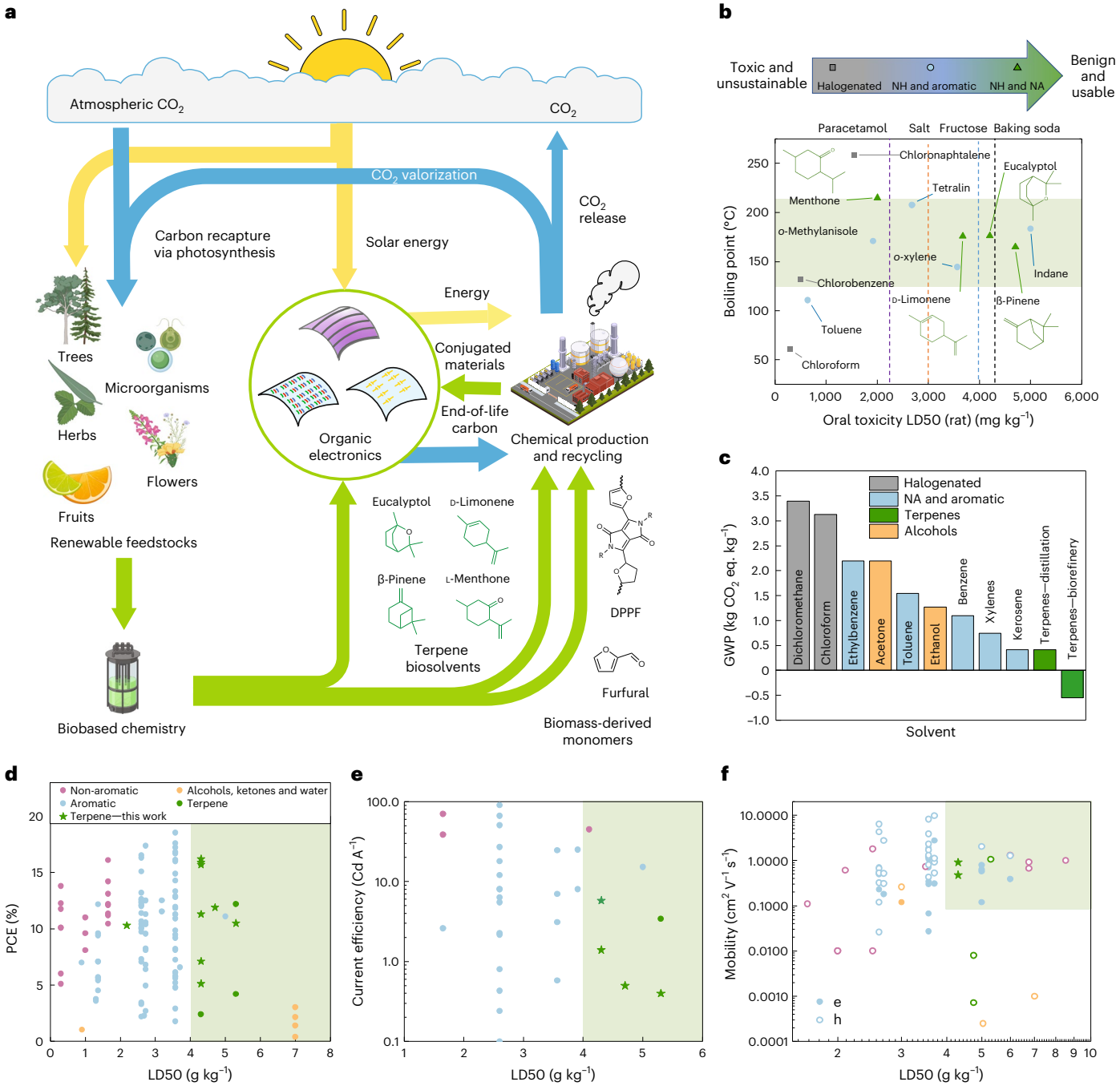

Fig. 1 | Toxicity and carbon footprint of solvents for OSCs. a, Schematic diagram showing the potential reduction of CO_2 emissions for organic electronic devices by circular carbon pathways including carbon valorization, recycling and carbon capture and utilization through renewable biomass feedstocks for terpene solvent production. **b**, Oral toxicity LD_{50} (rat), which refers to the toxicity measured with rats, versus boiling point of some of the most commonly used solvents for organic electronic devices including OPVs, OLEDs and OFETs and the proposed terpene green solvents. The coloured arrow denotes the transition from toxic and unsustainable halogenated solvents (grey squares) towards usable non-halogenated (NH) (blue circles) and non-aromatic (NA) solvents (green triangles). The four vertical dotted lines denote the toxicity of common compounds in medicine and food (paracetamol in purple, salt in orange, fructose in baby blue and baking soda in black), while the green shadowed area denotes the boiling point range for blade coating. **c**, Global warming potential (GWP) given in equivalent kg of CO_2 of different industrial solvents obtained from different life-cycle assessment studies and the ecoinvent life-cycle assessment database[24,25,27]. **d**, Oral toxicity LD_{50} versus power conversion efficiency of OPV devices focusing on the most notable works on green solvents divided by classification; the lime green shadowed zone presents areas of opportunity in research. **e**, LD_{50} versus current efficiency of OLED devices fabricated with green solvents. **f**, LD_{50} versus mobility of OFET devices fabricated with green solvents. An expanded form of these graphs is found in Supplementary Information and at www.omegalabresearch.com/resources. Panel **a** created partially with BioRender.com (images on the left).

solvent sits in the middle between the donor and acceptor in Hansen space (scenarios in Supplementary Information). This number in combination with RED (Supplementary Table 9) can help define how the film formation will occur upon evaporation of the ink solvents, which component will saturate first and the duration of crystallization. For instance, a higher A_{sol} and lower RED for a higher-BP solvent means the acceptor will remain in

https://doi.org/10.1038/s41560-022-01167-7

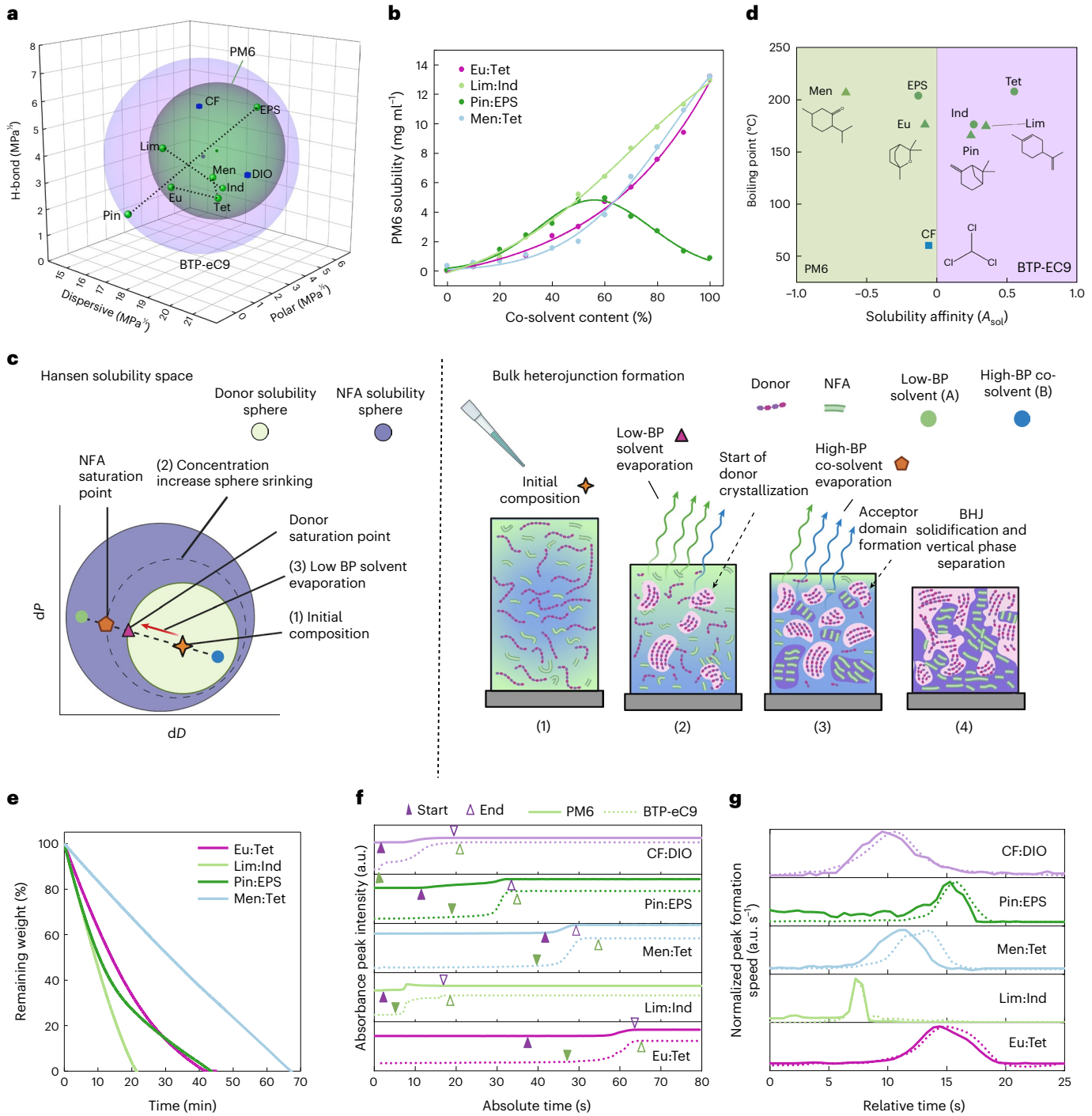

Fig. 2 | HSP-driven ink formulation and film formation mechanisms. a, 3D representation of the Hansen SSs of high-performing OPV materials, PM6 (green sphere) and BTP-eC9 (pink sphere). The position of the terpene solvents and co-solvents in Hansen space is denoted with green dots, while CF and DIO are presented in dark blue cubes. The binary solvent composition lines for the Eu:Tet, Lim:Ind, Pin:EPS and Men:Tet formulations are shown as dotted 'guides to the eye' in the diagram. **b**, PM6 solubility versus co-solvent content in each terpene-based formulation. The solubility profile aligns with Hansen binary composition lines. **c**, Diagram denoting the Hansen solubility binary solvent composition lines and the four stages of the bulk-heterojunction formation for organic photovoltaics. (1) First, the solution is deposited at the initial composition dictated by the closeness to the centre of the donor SS. (2) Second, as the low-BP terpene solvent evaporates, the overall concentration increases, shrinking the NFA SS to the point of saturation, where it begins crystallizing. (3) Then, as the higher-BP co-solvent starts evaporating, the formulation changes and moves across the solvent composition lines and reaches the edge of the NFA SS, where the donor domains start forming. (4) The remaining solvents keep evaporating until the final bulk heterojunction is formed. **d**, Solubility affinity of each solvent component versus boiling point. **e**, TGA evaporation curves denoting the remaining weight over time for a 10 µl droplet of each terpene-based formulation. **f**, In situ absorbance peak intensity versus absolute time tracking the formation of the PM6 (625 nm) and BTP-eC9 (830 nm) domains. The green and violet arrows represent the onset and end of solidification of PM6 and BTP-ec9, respectively. **g**, Normalized peak formation speed versus relative time of each formulation obtained by plotting the derivative of the normalized peak intensity over time (t). This derivative d(intensity)/dt explains how fast the absorbance peaks are forming and can provide a simplified view of the solidification process and its duration. These curves are superimposed next to one another to provide a better comparison at the film formation in relative time. The solid lines represent the formation of PM6, and the dotted lines, the formation of BTP-eC9. Panel **c** created with BioRender.com.

solution longer and will have more time to crystallize. The evaporation rate (ER), defined as the loss in mass over time, is presented through the thermogravimetric analysis (TGA) curves in Fig. 2e. The ER curves for pure solvents and binary inks follow Raoult's law of partial pressures (Supplementary Fig. 8)[34]. Solvent mixtures with higher-BP differences (Pin:EPS and Eu:Tet) result in two-stage curved ER lines, while formulations with similar vapour pressure and BP (Lim:Ind and Men:Tet) evaporate at constant rates[35]. The rise in concentration, saturation and crystallization is directly tied to the ER of the solvent constituents, and their solubility affinity towards either the donor or acceptor components.

We utilized blade coating, a compatible method for scale-up, optimized the deposition conditions and tracked the film formation dynamics for PM6 and BTP-eC9 in four terpene binary solvent inks alongside a CF control with 1,8-diiodooctane (DIO) through in situ absorbance measurements (Supplementary Fig. 9). At first, the PM6 and BTP-eC9 peaks in solution sit at around 600 nm and 740 nm, respectively. With solvent evaporation, the peak intensities decrease as a result of volume loss (ejection)[36]. Then, with preaggregation, the absorbance peaks for PM6 (~625 nm) and BTP-ec9 (~830 nm) first increase in prominence slowly for a few seconds, followed by an accelerated hike and ultimately reach a plateau, indicating a complete film solidification[37]. Figure 2f and Supplementary Fig. 10 track the peak formation from dissolved state to the solid state over time, while the speed of formation curves in Fig. 2g and Supplementary Fig. 11 provide a closer view for comparison.

The onset of solidification, the point where the peak formation speed starts increasing, begins earlier for BTP-eC9 in all formulations except Men:Tet. This is a confirmation of the loss in affinity for BTP-eC9 as terpene solvents evaporate and the corresponding SS begins to shrink. Likewise, the PM6 peaks reach their maximum earlier than BTP-eC9 for all formulations, signalling an early donor solidification. Although this process happens at a faster rate for Pin:EPS and Men:Tet. In contrast, Eu:Tet and CF:DIO inks show a slower peak formation for both donor and acceptor, denoting a slower crystallization that is finished at about the same time. It is worth noting that unoptimized blade coating temperature can result in unbalanced solidification of the components, lateral phase segregation and irregular film formation, while optimized conditions can yield more uniform films (Supplementary Fig. 12).

Photovoltaic performance of terpene-based formulations

We fabricated OPV devices for each terpene formulation via blade coating in air with the architecture shown in Fig. 3a. The PM6:BTP-eC9 photoactive layer (PAL) films went through judicious optimization of the co-solvent content (Supplementary Fig. 13) and blade coating parameters (Supplementary Fig. 14 and Supplementary Table 10). The utilization of HSP-optimized co-solvent content proved critical to donor–acceptor balance and device functionality. Starting Eu:Tet formulations at the edge of PM6 SS (~40% Tet content) produced barely functional devices, while higher co-solvent formulations resulted in reduced open circuit voltage (V_{oc}). Table 1 summarizes the optimized device photovoltaic parameters, while Fig. 3b compares the current density versus voltage (JV) curves of all terpene-based formulations. Devices from Eu:Tet and Pin:EPS inks demonstrated high short circuit current (J_{sc}) surrounding 25 mA cm^{-2} and V_{oc} values comparable to that of CF:DIO (0.83 V versus 0.84 V). In contrast, Lim:Ind and Men:Tet devices presented V_{oc} around 0.80 V and J_{sc} below 22.8 mA cm^{-2}, which can be attributed to modified local donor/acceptor content with drying kinetics and more prominent phase segregation. While the fill factor (FF) of Lim:Ind, Pin:EPS and Men:Tet devices surrounded 57% and permitted power conversion efficiencies (PCE) of up to 11.9%, devices from Eu:Tet ink exhibited a FF of 74% and astounding PCE values reaching 15.7%, which is among the highest values reported for green solvent inks and comparable to state-of-the-art CF:DIO devices[38].

The external quantum efficiency (EQE) response for Eu:Tet and Pin:EPS ink surrounds 80% (Fig. 3c). In comparison, Lim:Ind and Men:Tet devices denote a small dip between 400–600 nm, which may indicate a slight blend imbalance during drying. Additionally, the series resistance (R_s) for Eu:Tet (3.8 Ω) is slightly lower than that of CF:DIO (5.2 Ω), indicating a favourable vertical stratification ultimately improving the FF values[39]. The calculated slopes from the light intensity versus semi-logarithmic plot (Fig. 3d) are 1.02 K_BTq^{-1}, 1.07 K_BTq^{-1}, 1.22 K_BTq^{-1}, 1.03 K_BTq^{-1} and 1.62 K_BTq^{-1} for CF:DIO, Eu:Tet, Lim:Ind, Pin:EPS and Men:Tet, respectively, where K_B is the Boltzmann constant, T is the absolute temperature and q is the elementary charge. Devices from CF:DIO, Eu:Tet and Pin:EPS have slope values approaching unity, which indicates dominant non-geminate bimolecular recombination. Likewise, the α values for Eu:Tet and Pin:EPS (0.96) in the J_{sc} versus light intensity (P) plot in Fig. 3e suggest a weak bimolecular recombination and enhanced charge transport, ultimately improving the J_{sc} and FF[40].

The hole (μ_h) and electron (μ_e) mobilities of each ink formulation are calculated in Supplementary Fig. 15 and summarized in Supplementary Table 11 and Fig. 3f. The μ_h/μ_e ratio for Eu:Tet (1.66) is marginally higher than CF:DIO (0.98), while Pin:EPS and Lim:Ind present a ratio higher than 6. The slightly inferior μ_e and unbalanced μ_e/μ_h ratio (for other binary combinations) may generate from an enhanced crystallization of the polymer donor and reduced acceptor crystallization and unfavourable vertical phase stratification hindering charge transport[41,42]. In contrast, the more balanced evaporation, solubility affinity and RED ratio of Eu:Tet can produce less-isolated domains, more balanced charge transport, less recombination and higher FF values.

Formulation effect on morphology

To understand the rationale behind the performance resemblance of Eu:Tet and other terpene systems to CF:DIO, we performed atomic force microscope (AFM) (Fig. 4a) and grazing incidence wide angle X-ray scattering (GIWAXS) measurements. Men:Tet films showed elevated root mean square (RMS) values (29.66 nm) resulting from uneven drying and phase separation that was visible even at simple sight (Supplementary Fig. 12). In contrast, the fibrillar network morphology and RMS of Eu:Tet films resembling that of CF:DIO films (2.73 nm versus 1.36 nm) result from a more balanced PM6 aggregation and crystallization[43]. This blended nanoscale phase separation is favourable for light extraction and charge transport[44], thus explaining the improved mobility, J_{sc}, FF and overall device efficiency. Figure 4b shows the 2D GIWAXS pattern for PM6:BTP-eC9 films produced from different terpene-based inks, whereas the corresponding line-cut intensities taken along the in-plane (IP) and out-of-plane (OOP) directions are denoted in Fig. 4c,d. The films casted from Eu:Tet possess the most similar morphology to CF:DIO films (Supplementary Fig. 16), that is, intense 100 IP (~0.3 Å^{-1}) and 010 OOP (~1.75 Å^{-1}) peaks, which can be attributed to the donor and NFA species, respectively[29]. The integrated peak areas of the lamellar and π–π stacking (Fig. 4e) showcase the higher degree of crystallinity for the donor than the acceptor species in all terpene-based inks, which adheres to greater μ_h than μ_e values. Similarly, the higher degree of crystallinity for the acceptor in Eu:Tet films results from an equilibrated evaporation rate in combination with a slight affinity bias towards BTP-eC9 and yields a more balanced μ_h/μ_e ratio. Additionally, the surface energy characterization (Supplementary Fig. 17) demonstrates a higher surface concentration of BTP-eC9 for Eu:Tet films, contributing to higher μ_e, lower R_s and improvements in overall FF and performance in the conventional device architecture.

Universal and scalable manufacture of optoelectronics

We validate the upscaling potential of terpene biosolvents by fabricating PM6:BTP-eC9 devices over larger areas (0.33–2.4 cm^2) and solar modules with (12 cm^2 and 83% geometrical factor) with PCE values of up to 12% and 9.1%, respectively (Fig. 5a, Supplementary Fig. 18

https://doi.org/10.1038/s41560-022-01167-7

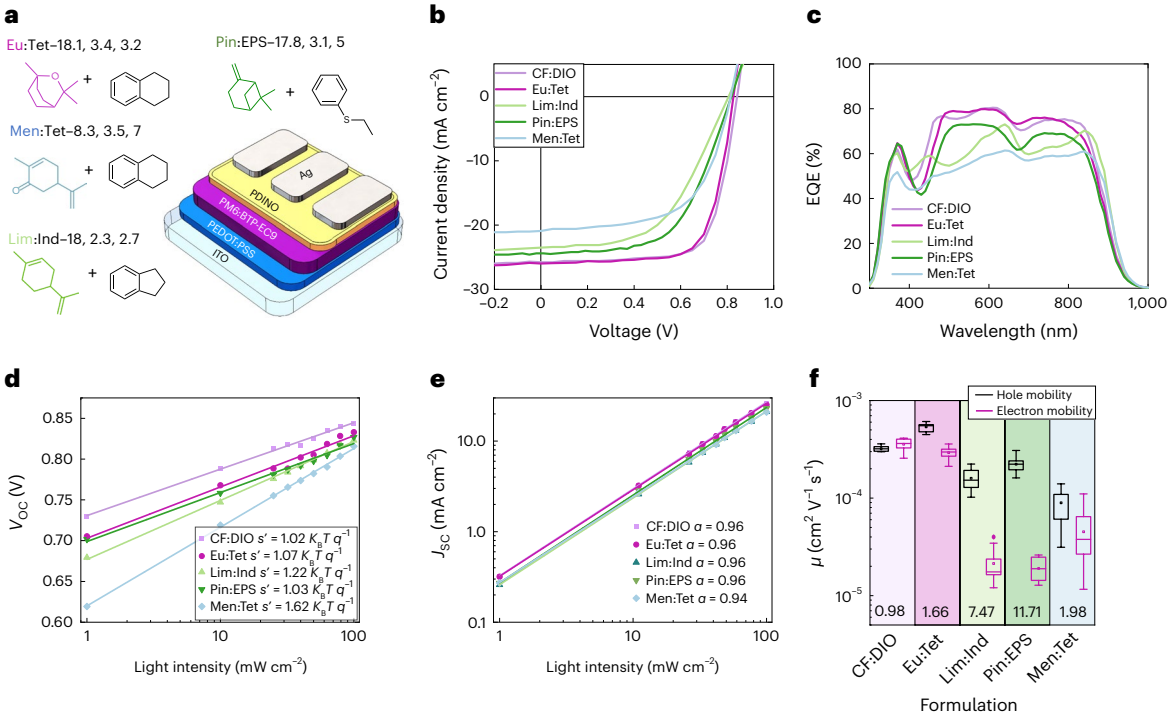

Fig. 3 | Photovoltaic performance of terpene formulations. a, Diagram denoting the device architecture ITO (light blue)/PEDOT:PSS (dark blue)/PM6:BTP:eC9 (pink)/PDINO (yellow)/silver (grey). The HSP values of each terpene-based formulation are given. Each coloured molecule represents the terpene for each formulation (Eu in pink, menthone in blue, Lim in lime green, Pin in dark green). The parentheses denotes the dispersive, polar and hydrogen-bond parameters in order (dD, dP, dH). **b**,**c**, JV curves (**b**) and EQE (**c**) comparing the performance of the blade coated devices in the normal architecture. The integrated J_{sc} calculated from EQE data have less than a 5% mismatch with JV measurements under a solar simulator. **d**, Semi-logarithmic plot of light intensity versus V_{oc} of the different terpene formulations. A higher slope (s') deviating from linearity and approaching $2\,K_BTq^{-1}$ indicates more pronounced trap-assisted recombination, where K_B is the Boltzman constant, T is temperature in degrees Kelvin and q is the elementary charge. **e**, Logarithmic plot of light intensity versus J_{sc} plot given by the relationship $J_{sc} \propto P^{\alpha}$, where α is the power law exponent and is given by the slope of each curve. Linear fits ($y = mx + b$) for **e** and **f** are given for $x = 1-100$ based on least squares approach. Pearson relation coefficient ($R > 0.999$). **f**, Comparison of electron (μ_e) and hole (μ_h) mobilities of hole-only and electron-only devices fabricated with the different terpene-based formulations as box plots (sample minimum, 25th percentile, median, 75th percentile and maximum) for $n = 15$ measurements. The average μ_h/μ_e ratio is given at the base of the plot.

Table 1 | Summary of photovoltaic parameters of PM6:BTP-eC9 devices fabricated in air at optimized conditions from different terpene-based formulations in the normal architecture

Formulation	J_{sc} (mA cm^{-2})	V_{oc} (V)	FF (%)	PCE (%)	PCE$_{max}$ (%)
CF:DIO	25.9±1.12	0.84±0.01	72±3.6	15.6±0.39	15.9
Eu:Tet	25.7±0.84	0.82±0.02	72±2.1	15.1±0.37	15.7
Lim:Ind	22.8±0.96	0.81±0.02	50±3.4	9.8+0.65	10.5
Pin:EPS	24.2±1.11	0.82±0.01	54±3.1	10.3+0.84	11.9
Men:Tet	20.8±0.76	0.79±0.01	58±1.9	9.7+0.21	10.3

The blade coating parameters of the different layers were optimized independently. CF:DIO devices were obtained through spin coating in nitrogen conditions. The values are the average representation of 12 pixels; standard deviation is given.

and Table 2). These devices retained up to 92% of their initial performance under nitrogen conditions and 60% under ambient humidity (ISOS-D-1) after 1,000 hours (Supplementary Fig. 19). Additionally, encapsulated devices retained their performance for up to 90 days (February–May 2022) under real-life outdoor conditions in Thuwal, Saudi Arabia (Fig. 5b), making it among the first reported outdoor results for Y series NFA and proving their viability for large-scale operation. We prove the universality of terpene-based inks for OPVs by calculating the HSP (Supplementary Table 12 and Supplementary Fig. 20), adapting the Eu:Tet formulation (Supplementary Fig. 21) and producing P3HT:O-IDTBR, PBT7-Th:IEICO-4F, PM6:IT-4F all polymer PM6:PY-IT binary devices with efficiencies comparable to that of chlorinated solvent counterparts (Fig. 5d–f and Table 2)[39,45–49]. Ternary PM6:(PYT:BTP-eC9) devices exhibited an impressive PCE of 16.3%, sitting among the highest values reported for green solvent inks so far. Lastly, we produced Super Yellow and green Livilux polymer-based OLEDs with high current efficiencies (5.1 cd A) and luminance values (9,000 cd m^{-2}) (Supplementary Fig. 22, Fig. 5d–f and Supplementary Video 1) and O-IDTBR and 2PyDPP-2CNTVT OFETs with mobilities approaching 1 cm^2 V^{-1} s^{-1} (Supplementary Fig. 23 and Fig. 5g–i) from pure Eu inks (Table 3 and Supplementary Table 13), on par with previously reported values for CF and Tol solvents[13,50].

Conclusion

We proposed the utilization of terpene solvents from renewable biosources as a low-toxicity, carbon-negative alternative to halogenated solvents for several high-performing organic electronic devices. The ink formulation framework extends the functionality of HSP binary solvent compositions to track the film formation mechanisms upon drying. We find that a terpene biosolvent with a balanced solubility affinity in combination with an acceptor affinity-biased high-BP co-solvent is required for producing a favourable morphology for high-performing OPV devices. This formulation strategy was deemed scalable over large areas and universal to a wide variety of polymer materials and NFAs in OPVs, OLEDs

https://doi.org/10.1038/s41560-022-01167-7

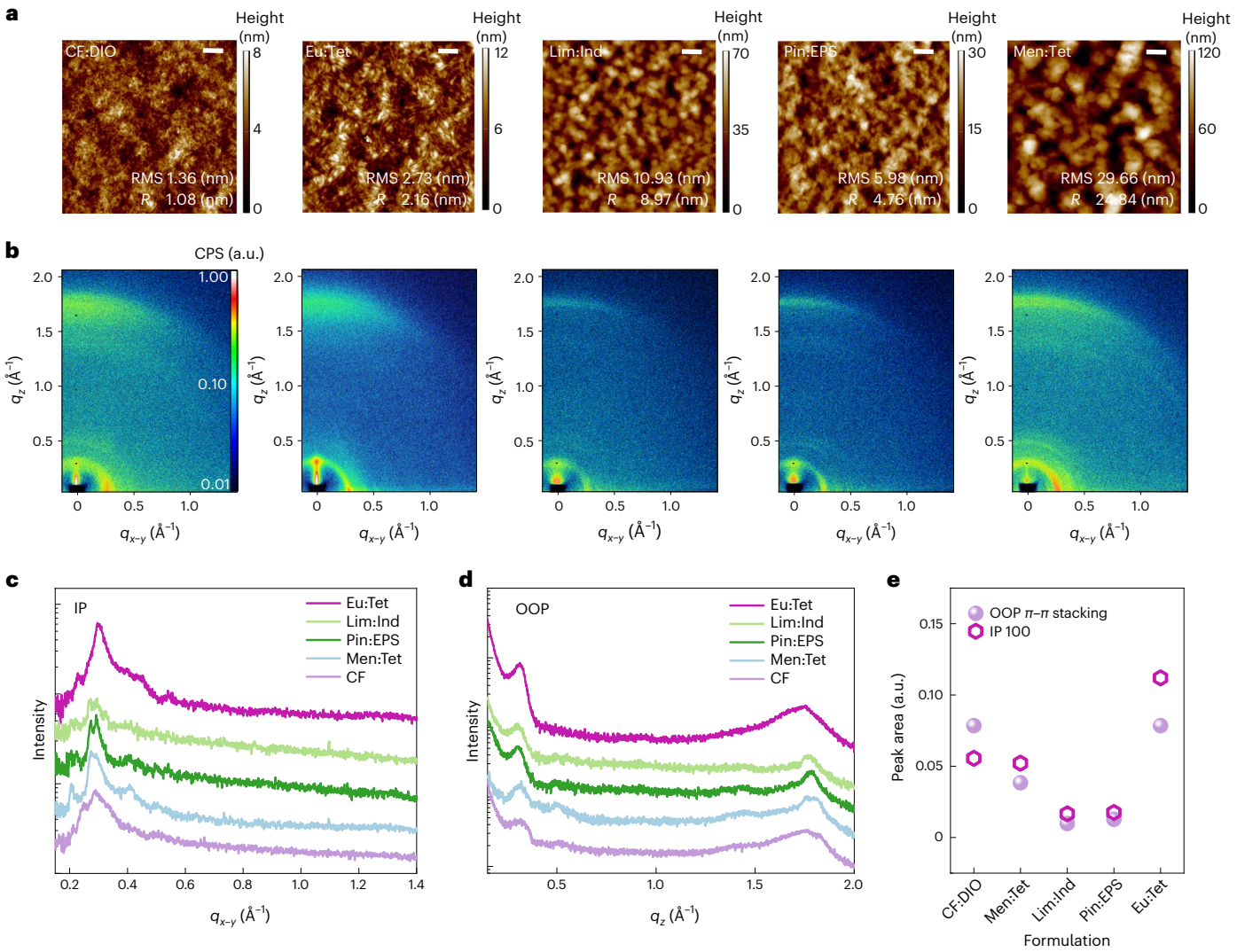

Fig. 4 | Morphological characterization. a,**b**, AFM height images (**a**) and 2D GIWAXS patterns (**b**) of the films obtained from different terpene-based formulations and CF:DIO. Scale bar in AFM images is 250 nm. $q_{x\text{-}y}$ and q_z denote X-ray scattering in the IP and OOP directions. CPS, counts per second. **c**,**d**, Corresponding GIWAXS profiles in the IP (**c**) and OOP (**d**) directions. **e**, Integrated peak area in the OOP and IP directions comparing the crystallinity for the donor (100 lamellar) and acceptor species (π–π stacking) for each terpene-based formulation.

and OFETs. Our findings for reduced carbon footprint solvent selection (made available at www.omegalabresearch.com/resources) highlight renewable terpenes such as carvone and linalool alongside anisole and γ-valerolactone for future studies. The compliance across safety, health and environmental impact categories alongside comprehensive life-cycle assessment reports can pave the way for truly green circular carbon initiatives for state-of-the-art OSC manufacturing processes.

Methods

Materials and ink formulation

Indium tin oxide (ITO) coated glass substrates were purchased from Xin Yan Technology HK. Menthone (Men) and ethyl phenyl sulfide (EPS) were purchased from Alfa Aeser. Eucalyptol (Eu), limonene (Lim), pinene (Pin) and all other solvents were purchased from Sigma–Aldrich and used as received. For the PAL, PM6 and BTP-eC9 (1-Material) were mixed in a (1:1.2) donor to acceptor ratio at a 10 mg ml^{-1} concentration and dissolved in 1 ml of each of the ink formulations Eu:Tet (52:48), Pin:EPS (55:45), Lim:Ind (58:42), Men:Tet (55:45). For the hole transport layer, PEDOT:PSS (Clevios AL4083) was sonicated for 10 minutes and filtered through a 1.2 µm PTFE filter before usage. For the electron transport layer, PDINO was dissolved in methanol at a 1.5 mg ml^{-1} concentration. For the ZnO sol-gel ink, we mixed zinc acetate dehydrate with ethanolamine (21 µl) and 2-methoxyethanol solution (1 ml).

Solar cell fabrication

The ITO coated glass substrates were cleaned in detergent, deionized water, acetone and IPA by sonication, followed by oxygen plasma treatment to remove organic residues. Conventional architecture devices had an ITO/PEDOT:PSS (30 nm)/PM6:BTP-eC9 (120 nm)/PDINO (5 nm)/Ag (100 nm) stack and were fabricated as follows. First the PEDOT:PSS solution was spin coated at 4,000 r.p.m. for 30 s and annealed at 160 °C for 10 minutes. The PAL was deposited in air through blade coating at different speeds ranging from 5 mm s^{-1} to 50 mm s^{-1} and temperatures ranging from 20 °C to 90 °C; the optimized parameters are listed in Supplementary Table 4. Then, the PDINO solution was spin coated at 3,000 r.p.m. for 30 seconds in a nitrogen atmosphere, followed by thermal evaporation of 100 nm of silver through a shadow mask. Inverted architecture devices (single cells and modules) had an (ITO/ZnO(25 nm)/PM6:BTP-eC9 (120 nm)/MoO_3 (10 nm)/Ag(100 nm)) stack and were fabricated as follows. First, the ZnO sol-gel solution was spin coated at

https://doi.org/10.1038/s41560-022-01167-7

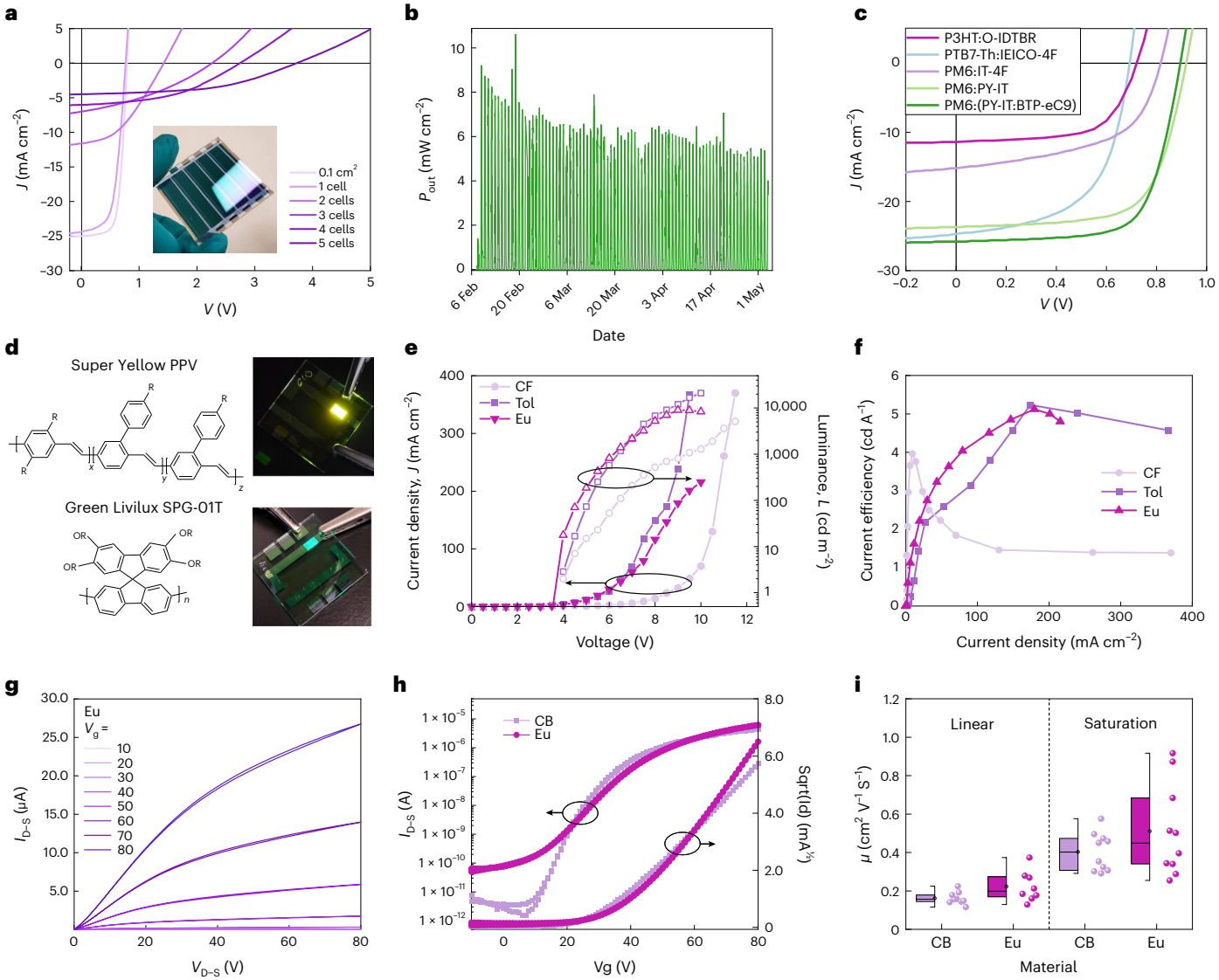

Fig. 5 | Scalability and universal terpene usage. a, JV curves of PM6:BTP-eC9 large area and modules made up of one to five single cell devices (2.4 cm^2) connected in series for a total area of 12 cm^2. Inset: photograph of a five-cell large-area module. **b**, Outdoor stability of PM6:BTP-eC9 large-area device. **c**, JV curves of OPV devices based on state-of-the-art blends: P3HT:O-IDTBR (inverted), PTB7-Th:IEICO-4F (inverted), PM6:IT-4F (inverted), PM6:PY-IT (normal) and PM6:(PY-IT:BTP-eC9) fabricated through blade coating in ambient conditions from Eu:Tet inks. **d**, Molecular structures and images of polymer OLEDs fabricated from Eu-based inks. **e**, JV and luminance curves of Super Yellow devices fabricated from different solvents. **f**, Current efficiency versus current density of Super Yellow OLED devices. **g**,**h**, Output curves (**g**) and transfer (**h**) curves of O-IDTBR-based OFET devices from CF and Eu inks. V_{D-S} and I_{D-S} are the drain–source voltage and current, respectively. V_{G-S} is the gate voltage and μ is the charge mobility. Sqrt refers to the square root. CB refers to chlorobenzene. **i**, Comparison of mobility of devices fabricated from CF and Eu in the linear and saturation regimes represented as box plots (sample minimum, 25th percentile, median, 75th percentile and maximum) for $n = 12$.

4,000 r.p.m. for 30 s and annealed at 200 °C for 10 minutes to achieve a layer thickness of 40 nm. Then, the PAL (120 nm) was blade coated as described above. Then, lastly, 10 nm of MoO_3 and 100 nm of silver were deposited at specific areas through a shadow mask through thermal evaporation. All devices had an area of 0.1 cm^2, except where specified. Large-area devices were defined following the same procedure and utilizing an evaporation mask with predefined areas (0.1–2.4 cm^2). Modules were fabricated by patterning the ITO layer with a Yb-fibre laser (P1 Line), utilizing a scribing guide to remove material to allow for series connection (P2 Line) and a custom evaporation mask (P3 Line).

OLED fabrication

Super-green and Super Yellow materials were dissolved overnight at 85 °C in Eu at 2.5 mg ml^{-1}. The ITO coated glass substrates were cleaned as described above. The conventional architecture devices were fabricated as follows. First, the Al 4083 PEDOT:PSS solution was spin coated at 4,000 r.p.m. for 30 s and annealed at 160 °C for 10 minutes. The PAL was deposited in air through blade coating at an optimized speed of 20 mm s^{-1}, followed by thermal evaporation of 10 nm of Ca and 100 nm of Al.

OFET fabrication

Devices were fabricated in a bottom-contact top-gate configuration by evaporating 50 nm of gold on a glass substrate through a shadow mask to define source and drain contacts; channel lengths ranged from 30 μm to 100 μm. This was followed by solution deposition of the OSC film. CYTOP CTL-809M was spin coated at 2,500 r.p.m. and dried at 90 °C for 20 minutes, yielding a dielectric layer of 1 μm. Lastly, a 40 nm Al contact was deposited by thermal evaporation. O-IDTBR films were

Table 2 | Summary of photovoltaic parameters of large-area single cell, module and devices from different PAL blends fabricated from Eu:Tet inks

Blend	Device area	Architecture	J_{sc} (mA cm^{-2})	V_{oc} (V)	FF (%)	PCE (%)	PCE$_{max}$ (%)	PCE$_{Rep}$ (%)
PM6:BTP-eC9	0.1 cm^2	Inverted	24.5±1.0	0.77±0.01	69±2.2	13.4±0.7	14.4	17.4[a] (ref. [38])
	2.4 cm^2	Inverted	22.8±2.3	0.77+.02	63±3.2	11.4±0.8	12.4	16.2[a,b] (ref. [38])
	12 cm^2 (Module)	Inverted	4.4±0.3	3.71±0.07	52±1.7	8.3±0.7	9.1	NA
PM6:PY-IT (1:1.2)	0.1 cm^2	Normal	23.8±0.9	0.92±0.02	70±2.3	15.7±0.3	15.9	15.8 (ref. [49])
PM6:(PY-IT:BTP-eC9) (1:0.9:0.1)	0.1 cm^2	Normal	25.3±0.5	0.90±0.01	71±1.1	16.1±0.2	16.3	16.2 (ref. [48])
PTB7-Th:IEICO-4F (1:1.5)	0.1 cm^2	Inverted	24.7±0.8	0.69±0.01	59±0.8	9.8±0.3	10.6	12.1 (refs. [39,40])
P3HT:O-IDTBR (1:1)	0.1 cm^2	Inverted	11.3±0.7	0.72±0.01	59±3.4	5.1±0.2	5.3	6.1 (ref. [45])
PM6:IT-4F (1:1.2)	0.1 cm^2	Inverted	19.4±1.6	0.83±0.02	57±1.9	8.2±0.8	9.2	12.1 (ref. [47])

Devices from PM6:PY-IT, PM6:(PY-IT:BTP-eC9) and PTB7-Th:IEICO-4F blends are the average representation of 12 pixels at optimized conditions. Devices of P3HT:O-IDTBR and PM6:IT-4F are the representation of six pixels produced as a first run but require further optimization. The last column (PCE$_{Rep}$) denotes the PCE values reported in literature for each blend. NA means not applicable. [a]Normal architecture. [b]1 cm^2 area.

Table 3 | Summary of characteristics of OLED and OFET devices fabricated from Eu inks and compared to CF- and CB-based devices

OLED material	Solvent	V_{on} (V)	Coordinates	L_{max} (Cd m^{-2})	CE$_{max}$ (Cd A^{-1})
Super Yellow	Eu	4.0	0.45,0.53	9,000	5.1
	CF	4.1	0.45,0.54	5,125	3.9
	Tol	4.5	0.45,0.52	41,000	5.2
Green Livilux	Eu	4.0	0.33,0.58	4,144	1.4
	CF	3.5	0.26,0.58	8,217	1.5
	Tol	3.8	0.27,0.58	3,144	1.2

OFET material	Solvent	V_{Th} (V)	Max μ_{Lin} (cm^{2}V^{-1}s^{-1})	Max μ_{Sat} (cm^{2}V^{-1}s^{-1})	I_{on}/I_{off}
O-IDTBR	CB	35.0	0.22	0.57	>10^5
	Eu	38.8	0.37	0.91	>10^5
2PyDPP-2CNTVT	CB	42.8	0.15	0.21	>10^5
	Eu	38.6	0.32	0.48	>10^4

blade coated from a 2.5 mg ml^{-1} solution in Eu at 30 mm s^{-1} and 90 °C bed temperature to achieve 50 nm thickness. 2PyDPP-2CNTVT films were blade coated from a 2 mg ml^{-1} solution in Eu at 10 mm s^{-1} and 90 °C to achieve a 20 nm thickness.

Photovoltaic characterization

The current density–voltage (JV) curves were obtained by simulating the solar spectrum at AM 1.5 illumination through a 21 LED engine (Wavelabs Sinus-70) in a N_2 environment and using a voltage sweep from −1 V to 1 V in 0.02 V intervals while measuring the resulting current with a Keithley 2400 source meter. The instrument was calibrated with a certified 91,150 V silicon reference cell from Newport. The light intensity versus open circuit voltage (V_{oc}) and short circuit current (J_{sc}) measurements were carried out with neutral density optical filters (Thorlabs) ranging from optical density (OD) 0.1 to 4. The transmitted light can be calculated through the formula $T = 10^{-OD}$, where T is a value between 0 and 1.

EQE

The EQE curves were obtained using a 75 W Xenon lamp along with a chopper and monochromator (Enlitech QE-R); the instrument was calibrated using a silicon photodiode. The EQE response demonstrated less than 5% mismatch in comparison with solar simulator response.

Stability characterization

Shelf-life measurements were performed by taking the JV curves as specified above at specified time intervals in a N_2 glovebox. The devices were kept in N_2 under dark and ambient humidity (50–65% relative humidity) at room temperature (ISOS-D1 Protocol). Devices were prepared for outdoor testing with a vacuum-laminated encapsulant and edge sealing via butyl rubber. Outdoor measurements were performed on a roof clear of any obstacles keeping the devices at open circuit and taking the corresponding JV curves in 10-minute intervals from 6 February 2022 to 7 May 2022.

Space charged limited current

Hole-only devices and electron-only devices were fabricated with the same methodology described above with the architecture (ITO/PEDOT:PSS(30 nm)/PM6:BTP-eC9(120 nm)/Al(100 nm)) and (ITO/ZnO(30 nm)/PM6:BTP-eC9(120 nm)/PFN-Br(5 nm)/Al(100 nm)) to measure the hole (μ_h) and electron (μ_e) mobilities. The current was measured in the dark while doing voltage sweeps from −3 V to 3 V, −5 V to 5 V and −8 V to 8 V to find the area where the slope of the JV log curve is equal to 2.

Evaporation characterization

To assess the evaporation rate, we placed a 10 µl droplet of each solvent and solvent formulations in an aluminium crucible separately and allowed it to evaporate over the course of 45 minutes while measuring the mass loss through a NETZCH STA 449 Jupiter Thermogravimetric Analysis instrument (TGA) at 70 °C and a nitrogen flow of 20 sccm (standard cubic centimetres per minute).

Solubility characterization

To find the solubility limit of PM6 and BTP-eC9 in each of the solvents, small amounts of each component were added in 0.1–0.2 mg increments in 1 ml of each solvent/solvent mixture heated at 70 °C for 15 minutes and then cooled down for 15 minutes to room temperature (21 °C). The procedure was repeated until signs of precipitation occurred, which is considered the solubility limit. Heating and cooling temperatures were confirmed via a non-contact infrared thermometer (Fluke 62 Max).

Determination of Hansen solubility parameters

The HSP values of PAL materials were determined according to the binary solvent gradient methodology by utilizing chlorobenzene, propylene carbonate and non-solvents octane, 1-pentanol and propylene carbonate and finding the solubility limit at each composition according to the method stated above. The regression of the SS for each material was performed on the HSPiP software by denoting a value of 1 to all gradient compositions that reached a concentration of 5 mg ml^{-1} without forming any visible aggregates and a 0 to those which did not.

The HSP values for the list of solvents in Supplementary Table 5 were obtained from the HSPiP database.

OLED characterization
Current–voltage characteristics were measured from Keithley source meter 2400 supplied from Tektronix. Brightness was captured using a Konica Minolta CS-2000 spectrometer purchased from Konica Minolta. Electroluminescence spectrum was captured by supplying the d.c. voltage bias of 7 V through with source meter (model: Keithley 2420 supplied from Tektronix). Light from OLEDs was collected by a collimator and sent to the spectrograph, supplied by Princeton Instruments SP-2300, through an optical fibre. The spectrometer consists of a cooled Si (PIX100BRX) and cooled InGaAs (PYR1024) detector array.

OFET characterization
Transfer and output curves were measured using a Keithley 4200-SCS connected to a probe station within a N_2-filled glove box. Linear transfer curves were obtained at $V_{D-S} = 10$ V, while saturation curves were measured at $V_{D-S} = 80$ V.

Contact angle measurements
The surface energy components and wetting envelope of the different films were calculated by using the Owens, Wendt, Rabel and Kaelble methodology through the measurement of the sessile drop contact angle of three different liquids (water, ethylene glycol, diiodomethane) on the selected surface with a Kruss DSA100 drop shape analyser.

Steady-state absorbance spectroscopy
The UV–vis absorbance spectra was obtained through a Perkin Elmer spectrophotometer with an integrating sphere by varying the wavelengths of the light beam from 350 nm up to 100 nm at 2 nm intervals.

In situ absorbance spectroscopy
A F20-UVX spectrometer (Filmetrics) equipped with tungsten halogen *f* and deuterium light sources (Filmetrics) was mounted on a Zehntner blade coater to measure the absorbance of the wet films as they dried over the 350 nm to 1,100 nm wavelength range. The measurements were performed with an integration time of 0.05 s per spectrum sweep measurement.

Surface energy characterization
A drop shape analyser (DSA100) is used to deposit and measure the sessile drop contact angle of three different liquids (water, ethylene glycol, diiodomethane) on the selected surface. The calculation of the polar and dispersive components and wetting envelope was done by following the Owens, Wendt, Rabel and Kaelble methodology.

Microscopy imaging
Optical microscopy images were obtained on a Nikon Eclipse LV100POL microscope with 50×, 20×, 10× and 5× objectives paired with a Nikon DS-F11 camera.

AFM measurements
AFM images were captured using the solver-next scanning probe microscope (NT-MDT) equipped with an OTESPA cantilever (Bruker) and measured over different square areas ranging from 2 µm to 20 µm per side.

GIWAXS measurements
GIWAXS data were collected in a D8 Discover (Bruker) equipped with a lµS CuKα source (λ = 1.54 Å) and an Eiger 2 R 500 K detector mounted on a goniometer. The incidence angle was optimized at 0.14°. Total collection time was 1.7 hours per sample.

Profilometry measurements
The thickness of the films was measured through a stylus mechanical profilometer (Tencor P7) by applying a 0.5 mN force on the probing tip.

Reporting summary
Further information on research design is available in the Nature Portfolio Reporting Summary linked to this article.

Data availability
All data supporting the findings of this study are available within the article and its Supplementary Information and source data files. The device performance comparison, Hansen solubility parameters database for different solvents and the GSK calculation spreadsheet are available in the Supplementary Information and at www.omegalabresearch.com/resources. Source data are provided with this paper.

References

1. Riede, M., Spoltore, D. & Leo, K. Organic solar cells—the path to commercial success. *Adv. Energy Mater.* **11**, 2002653 (2021).
2. Phan, S. & Luscombe, C. K. Recent advances in the green, sustainable synthesis of semiconducting polymers. *Trends Chem.* **1**, 670–681 (2019).
3. Cui, Y. et al. Single-junction organic photovoltaic cell with 19% efficiency. *Adv. Mater.* **33**, 2102420 (2021).
4. Romashov, L. V. & Ananikov, V. P. Alkynylation of bio-based 5-hydroxymethylfurfural to connect biomass processing with conjugated polymers and furanic pharmaceuticals. *Chem. Asian J.* **12**, 2652–2655 (2017).
5. Burke, D. J. & Lipomi, D. J. Green chemistry for organic solar cells. *Energy Environ. Sci.* **6**, 2053–2066 (2013).
6. Fang, X. et al. Rapid increase in ozone-depleting chloroform emissions from China. *Nat. Geosci.* **12**, 89–93 (2019).
7. Mattock, H. *IARC Monographs on the Evaluation of Carcinogenic Risks to Humans* (International Agency for Research on Cancer, 2022).
8. Zhao, J. et al. Efficient organic solar cells processed from hydrocarbon solvents. *Nat. Energy* **1**, 15027 (2016).
9. Kim, C. et al. Green solvent-processed, high-performance organic solar cells achieved by outer side-chain selection of selenophene-incorporated Y-series acceptors. *J. Mater. Chem. A* https://doi.org/10.1039/D1TA07046K (2021).
10. Dayneko, S. V. et al. Improved performance of solution processed OLEDs using *N*-annulated perylene diimide emitters with bulky side-chains. *Mater. Adv.* **2**, 933–936 (2021).
11. Du, B. et al. Hot-casting boosts efficiency of halogen-free solvent processed non-fullerene organic solar cells. *Adv. Funct. Mater.* **31**, 2105794 (2021).
12. Lee, M. et al. Green solvent-processed complementary-like inverters based on ambipolar organic thin-film transistors. *J. Ind. Eng. Chem.* **105**, 231–237 (2022).
13. C, A., Szymański, M. Z., Łuszczyńska, B. & Ulański, J. Inkjet printing of Super Yellow: ink formulation, film optimization, OLEDs fabrication, and transient electroluminescence. *Sci. Rep.* **9**, 8493 (2019).
14. Machui, F., Langner, S., Zhu, X., Abbott, S. & Brabec, C. J. Determination of the P3HT:PCBM solubility parameters via a binary solvent gradient method: impact of solubility on the photovoltaic performance. *Sol. Energy Mater. Sol. Cells* **100**, 138–146 (2012).
15. Sprau, C. et al. Green inks for the fabrication of organic solar cells: a case study on PBDTTPD:PC61BM bulk heterojunctions. *Adv. Energy Sustainability Res.* **2**, 2100043 (2021).
16. Ye, L. et al. Sequential deposition of organic films with eco-compatible solvents improves performance and enables over 12%-efficiency nonfullerene solar cells. *Adv. Mater.* **31**, 1808153 (2019).
17. Sanchez-Lengeling, B. et al. A Bayesian approach to predict solubility parameters. *Adv. Theor. Simul.* **2**, 1800069 (2019).

18. Lambourne, R. in *Paint and Surface Coatings* 2nd edn (eds Lambourne, R. & Strivens, T. A.) 166–184 (Woodhead Publishing, 1999).
19. Novo, L. P. & Curvelo, A. A. S. Hansen solubility parameters: a tool for solvent selection for organosolv delignification. *Ind. Eng. Chem. Res.* **58**, 14520–14527 (2019).
20. Wu, H. et al. Effect of hydrodistillation on 1,8-cineole extraction from mallee leaf and the fuel properties of spent biomass. *Ind. Eng. Chem. Res.* **50**, 11280–11287 (2011).
21. Della Monica, F. & Kleij, A. W. From terpenes to sustainable and functional polymers. *Polym. Chem.* **11**, 5109–5127 (2020).
22. Mewalal, R. et al. Plant-derived terpenes: a feedstock for specialty biofuels. *Trends Biotechnol.* **35**, 227–240 (2017).
23. Breitmaier, E. *Terpenes: Flavors, Fragrances, Pharmaca, Pheromones* Ch. 1 (Wiley, 2006).
24. Ciriminna, R., Lomeli-Rodriguez, M., Demma Carà, P., Lopez-Sanchez, J. A. & Pagliaro, M. Limonene: a versatile chemical of the bioeconomy. *Chem. Commun.* **50**, 15288–15296 (2014).
25. Wernet, G. et al. The ecoinvent database version 3 (part I): overview and methodology. *Int. J. Life Cycle Assess.* **21**, 1218–1230 (2016).
26. Lauersen, K. J. Eukaryotic microalgae as hosts for light-driven heterologous isoprenoid production. *Planta* **249**, 155–180 (2019).
27. Jahandideh, A. et al. Life cycle analysis of a large-scale limonene production facility utilizing filamentous N_2-fixing cyanobacteria. *Algal Res.* **23**, 1–11 (2017).
28. Zhang, D., del Rio-Chanona, E. A., Wagner, J. L. & Shah, N. Life cycle assessments of bio-based sustainable polylimonene carbonate production processes. *Sustain. Prod. Consum.* **14**, 152–160 (2018).
29. Cai, Y. et al. A well-mixed phase formed by two compatible non-fullerene acceptors enables ternary organic solar cells with efficiency over 18.6%. *Adv. Mater.* **33**, 2101733 (2021).
30. Zhang, S., Ye, L., Zhang, H. & Hou, J. Green-solvent-processable organic solar cells. *Mater. Today* **19**, 533–543 (2016).
31. Hansen, C. M. *Hansen Solubility Parameters: A User's Handbook* (CRC Press, 2007).
32. Larsen, C. et al. A tool for identifying green solvents for printed electronics. *Nat. Commun.* **12**, 4510 (2021).
33. Alder, C. M. et al. Updating and further expanding GSK's solvent sustainability guide. *Green Chem.* **18**, 3879–3890 (2016).
34. Corzo, D. et al. A universal cosolvent evaporation strategy enables direct printing of perovskite single crystals for optoelectronic device applications. *Adv. Mater.* **34**, 2109862 (2022).
35. Mackay, D. & van Wesenbeeck, I. Correlation of chemical evaporation rate with vapor pressure. *Environ. Sci. Technol.* **48**, 10259–10263 (2014).
36. Abdelsamie, M., Zhao, K., Niazi, M. R., Chou, K. W. & Amassian, A. In situ UV–visible absorption during spin-coating of organic semiconductors: a new probe for organic electronics and photovoltaics. *J. Mater. Chem.* **2**, 3373–3381 (2014).
37. Lin, B. et al. Balancing the pre-aggregation and crystallization kinetics enables high efficiency slot-die coated organic solar cells with reduced non-radiative recombination losses. *Energy Environ. Sci.* **13**, 2467–2479 (2020).
38. Cui, Y. et al. Single-junction organic photovoltaic cells with approaching 18% efficiency. *Adv. Mater.* **32**, 1908205 (2020).
39. Corzo, D., Bihar, E., Alexandre, E. B., Rosas-Villalva, D. & Baran, D. Ink engineering of transport layers for 9.5% efficient all-printed semitransparent nonfullerene solar cells. *Adv. Funct. Mater.* **31**, 2005763 (2021).
40. Song, X. et al. Controlling blend morphology for ultrahigh current density in nonfullerene acceptor-based organic solar cells. *ACS Energy Lett.* **3**, 669–676 (2018).
41. Zhang, Y. et al. Graded bulk-heterojunction enables 17% binary organic solar cells via nonhalogenated open air coating. *Nat. Commun.* **12**, 4815 (2021).
42. Bi, S., Ouyang, Z., Shaik, S. & Li, D. Effect of donor–acceptor vertical composition profile on performance of organic bulk heterojunction solar cells. *Sci. Rep.* **8**, 9574 (2018).
43. Zhu, L. et al. Single-junction organic solar cells with over 19% efficiency enabled by a refined double-fibril network morphology. *Nat. Mater.* **21**, 656–663 (2022).
44. Li, C. et al. Non-fullerene acceptors with branched side chains and improved molecular packing to exceed 18% efficiency in organic solar cells. *Nat. Energy* **6**, 605–613 (2021).
45. Corzo, D. et al. Digital inkjet printing of high-efficiency large-area nonfullerene organic solar cells. *Adv. Mater. Technol.* **4**, 1900040 (2019).
46. Liu, T. et al. 16% efficiency all-polymer organic solar cells enabled by a finely tuned morphology via the design of ternary blend. *Joule* **5**, 914–930 (2021).
47. Lin, Y. et al. 17.1% efficient single-junction organic solar cells enabled by n-type doping of the bulk-heterojunction. *Adv. Sci.* **7**, 1903419 (2020).
48. Song, W. et al. Entangled structure morphology by polymer guest enabling mechanically robust organic solar cells with efficiencies of over 16.5%. *Matter* **5**, 1877–1889 (2022).
49. Cui, F.-Z. et al. Ternary-assisted sequential solution deposition enables efficient all-polymer solar cells with tailored vertical-phase distribution. *Adv. Funct. Mater.* **32**, 2200478 (2022).
50. Paterson, A. F. et al. N-doping improves charge transport and morphology in the organic non-fullerene acceptor O-IDTBR. *J. Mater. Chem.* **9**, 4486–4495 (2021).

Acknowledgements

This publication is based upon work supported by the King Abdullah University of Science and Technology Office of Sponsored Research under award number CCF-3079.

Author contributions

D.C. and D.B. conceived the idea. D.C. conducted the work and wrote the manuscript. D.B. guided the work and wrote the manuscript. D.R.-V. performed AFM and GIWAXS characterization and OFET measurements. A.C. helped with solar cell and OLED fabrication and characterization. G.T.-B. and E.B.A. helped with solubility tests, in situ absorbance measurements and HSP determination. J.H. and H.X. helped with solar cell fabrication. M.B. and S.D.W. performed encapsulation, and L.H.H. set up outdoor stability characterization. All co-authors contributed to manuscript writing and editing.

Competing interests

The authors declare no competing interests.

Additional information

Supplementary information The online version contains supplementary material available at https://doi.org/10.1038/s41560-022-01167-7.

Correspondence and requests for materials should be addressed to Derya Baran.

Peer review information *Nature Energy* thanks Changduk Yang and the other, anonymous, reviewer(s) for their contribution to the peer review of this work.

nature research

Corresponding author(s): Derya Baran

Solar Cells Reporting Summary

Nature Research wishes to improve the reproducibility of the work that we publish. This form is intended for publication with all accepted papers reporting the characterization of photovoltaic devices and provides structure for consistency and transparency in reporting. Some list items might not apply to an individual manuscript, but all fields must be completed for clarity.

For further information on Nature Research policies, including our data availability policy, see Authors & Referees.

Experimental design

Please check: are the following details reported in the manuscript?

1. Dimensions

Area of the tested solar cells	☒ Yes ☐ No	The area for each device is specified methods section and Table 2.
Method used to determine the device area	☒ Yes ☐ No	Methods section Page 13: Solar Cell Fabrication

2. Current-voltage characterization

Current density-voltage (J-V) plots in both forward and backward direction	☐ Yes ☒ No	This OPV devices presented the same response in forward and backward direction
Voltage scan conditions *For instance: scan direction, speed, dwell times*	☒ Yes ☐ No	This information is stated in methods section: Photovoltaic Characterization
Test environment *For instance: characterization temperature, in air or in glove box*	☒ Yes ☐ No	This is stated in methods section: Photovoltaic Characterization
Protocol for preconditioning of the device before its characterization	☒ Yes ☐ No	Methods section Photovoltaic Characterization.
Stability of the J-V characteristic *Verified with time evolution of the maximum power point or with the photocurrent at maximum power point; see ref. 7 for details.*	☒ Yes ☐ No	Method section: Stability Characterization.

3. Hysteresis or any other unusual behaviour

Description of the unusual behaviour observed during the characterization	☐ Yes ☒ No	No Hysteresis was observed for these devices
Related experimental data	☐ Yes ☒ No	Not Applicable

4. Efficiency

External quantum efficiency (EQE) or incident photons to current efficiency (IPCE)	☒ Yes ☐ No	Figure 3c and Supporting Information.
A comparison between the integrated response under the standard reference spectrum and the response measure under the simulator	☒ Yes ☐ No	Caption of Figure 3 & methods section: EQE measurements.
For tandem solar cells, the bias illumination and bias voltage used for each subcell	☐ Yes ☒ No	No tandems were produced

5. Calibration

Light source and reference cell or sensor used for the characterization	☒ Yes ☐ No	Methods section Pg 13.
Confirmation that the reference cell was calibrated and certified	☒ Yes ☐ No	Method Section: Photovoltaic Characterization

Calculation of spectral mismatch between the reference cell and the devices under test	☐ Yes ☒ No	The LED solar simulator was calibrated to produce AM1.5 spectrum.

6. Mask/aperture

Size of the mask/aperture used during testing	☐ Yes ☒ No	The JV measurements were not performed with a mask, but rather a defined area. bottom electrode
Variation of the measured short-circuit current density with the mask/aperture area	☐ Yes ☒ No	The JV measurements were not performed with a mask.

7. Performance certification

Identity of the independent certification laboratory that confirmed the photovoltaic performance	☐ Yes ☒ No	No certification was obtained for these cells.
A copy of any certificate(s) *Provide in Supplementary Information*	☐ Yes ☒ No	Not applicable

8. Statistics

Number of solar cells tested	☒ Yes ☐ No	This is stated in the caption of each table.
Statistical analysis of the device performance	☒ Yes ☐ No	The statistical analysis is found in Supplementary Figure 12.

9. Long-term stability analysis

Type of analysis, bias conditions and environmental conditions *For instance: illumination type, temperature, atmosphere humidity, encapsulation method, preconditioning temperature*	☒ Yes ☐ No	This is stated in the text in page 10 , methods section, and the caption of Figure S17.